Research Article

Evaluation of stability and functionality of $BaCe_{1-x}In_xO_{3-\delta}$ electrolyte in a wider range of indium concentration

Aleksandar MALEŠEVIĆ[a,*], Aleksandar RADOJKOVIĆ[a], Milan ŽUNIĆ[a],
Aleksandra DAPČEVIĆ[b], Sanja PERAĆ[a], Zorica BRANKOVIĆ[a],
Goran BRANKOVIĆ[a]

[a]*Center of Excellence for Green Technologies, Institute for Multidisciplinary Research,*
University of Belgrade, Kneza Višeslava 1, 11030 Belgrade, Serbia
[b]*Faculty of Technology and Metallurgy, University of Belgrade, Karnegijeva 4, 11120 Belgrade, Serbia*

Abstract: The properties of $BaCe_{1-x}In_xO_{3-\delta}$ (x = 0.05, 0.10, 0.15, 0.20, 0.25, 0.30, 0.35, and 0.40) as proton conducting electrolyte are examined. The dense electrolyte is formed after sintering at 1300 ℃ for 5 h in air. The samples with In content $\geqslant$ 25 mol% contain In_2O_3 as a secondary phase. The highest total conductivity is around 5×10^{-3} S/cm for $BaCe_{0.75}In_{0.25}O_{3-\delta}$ in the wet hydrogen atmosphere at 700 ℃. After exposure to pure CO_2 atmosphere at 700 ℃ for 5 h, the concentrations of at least 15 mol% In can completely suppress degradation of the electrolyte. The power density of $Ni-BaCe_{0.75}In_{0.25}O_{3-\delta}/BaCe_{0.75}In_{0.25}O_{3-\delta}/LSCF-BaCe_{0.75}In_{0.25}O_{3-\delta}$ fuel cell tested in wet hydrogen atmosphere reaches 264 mW/cm^2 at 700 ℃. This result is an indication of stability and functionality of this electrolyte and its versatility in respect to type of fuel and performing environment.

Keywords: ionic conductivity; perovskite; fuel cell; $BaCeO_3$

1 Introduction

Proton conduction of mixed oxides with perovskite structure, at temperatures above 500 ℃, has been studied since the beginning of the 1980s [1–3]. $BaCeO_3$-based materials exhibited significant proton conductivity and high potential for their application in intermediate-temperature solid oxide fuel cells (IT-SOFC) [4]. In recent years, many attempts have been made to improve the properties of the most studied high-temperature proton conductor $BaCe_{0.90}Y_{0.10}O_{3-\delta}$ (BCY), particularly in terms of conductivity by replacing Y with rare earth elements [5–8] and stability in acidic environments by co-doping with cations of higher electronegativity [9–12]. Doping of $BaCeO_3$ with trivalent cations, that partially replace Ce^{4+} located in the center of an octahedron formed by oxygen ions, is charge balanced by emergence of oxygen vacancies $(V_O^{\bullet\bullet})$, whereby they take part in formation of proton defects $(OH_O^{\bullet})$ in wet or hydrogen containing atmospheres at elevated temperatures [13,14]. As ionic conductivity is directly proportional to the concentration of the charge carriers and their mobility, a relatively high concentration of proton defects itself is not enough to achieve fast proton conductivity at observed temperature. The mobility of the protons is very important

* Corresponding author.
E-mail: amalesevic@imsi.rs

and it depends on: (1) chemical factors: dopant valence and electronegativity, basicity of the oxygen ions; (2) structural factors: symmetry, dopant radius size, and unit cell volume; and (3) microstructure: grain size, porosity, etc. [15–17]. On the other hand, the main reason for instability in CO_2-rich atmosphere is the basic character of the crystal lattice, and overall stability of the structure defined by Goldschmidt tolerance factor, *t* [18]. It was previously found that the stability of BCY can be enhanced by doping with cations that may raise the acidic character of the material, such as Nb^{5+}, Ta^{5+}, or Zr^{4+} [9,10,19,20]. Introduction of these cations leads to reduced amount of point defects, increased acidity of the oxygen ions, and consequently lower proton conductivity. The process of doping has opposite effects on the conductivity and stability of an electrolyte, which could be compromised by a selective optimization of its properties. Therefore, it was suggested that an ideal replacement for Y^{3+} in BCY should be a trivalent, medium-sized ion with amphoteric character [21]. In that regard, In^{3+} seems suitable as it can completely replace Y^{3+} and serve both as point defect source and inhibitor of the electrolyte degradation caused by CO_2 [17,22–24]. Due to these properties, In^{3+} can be introduced in much larger amounts than Nb^{5+} or Ta^{5+}, while its relatively high electronegativity (1.78) may negatively affect proton mobility. Besides, In^{3+} was also found to promote sinterability of the ceramics at lower temperatures, which can moderate the strain on the anode/electrolyte interface induced by different thermal expansion coefficients of the electrolyte and NiO-based anode in an anode-supported fuel cell configuration [22–24]. Particularly in this type of fuel cell configuration, the assumed lower conductivity of In-doped $BaCeO_3$ electrolyte can be compensated by reducing its thickness. In this respect, much can be achieved by using an appropriate synthesis method and processing technique. For instance, the auto-combustion synthesis method regularly produces electrolyte powders with much higher specific surface area than the classic solid state reaction method [10,25,26]. Higher specific surface area of these powders make them more versatile for application of various processing techniques, such as co-pressing and co-sintering, spin coating, inkjet printing, electrophoresis, etc., which can produce very thin and uniform electrolyte layers, usually ~20 μm and even thinner [18,24,27]. The microstructure and dopant dispersion in bulk ceramics obtained by the auto-combustion method are more homogeneous, which is another advantage of this synthesis method. Thus, the so-called trade-off relationship between conductivity and stability can be biased towards higher conductivities sustaining the same degree of stability in CO_2.

Although previous investigations of properties of In-doped $BaCeO_3$ can be found in literature [22,23], in this paper, we studied the properties of $BaCe_{1-x}In_xO_{3-\delta}$ electrolyte in a wider range of dopant concentrations in order to determine the optimal In concentration for its application as an electrolyte for SOFCs. Furthermore, a detailed analysis of microstructure, crystal structure, and electrical properties was conducted with the aim of providing more profound insight in their correlation.

2 Materials and methods

$BaCe_{1-x}In_xO_{3-\delta}$ (x = 0.05, 0.10, 0.15, 0.20, 0.25, 0.30, 0.35, and 0.40) powders were synthesized by the auto-combustion reaction method and denoted as BCI5, BCI10, BCI15, BCI20, BCI25, BCI30, BCI35, and BCI40, respectively. Barium(II) nitrate (Fluka, min. 99.0%), cerium(III) nitrate hexahydrate (Fluka, min. 99.0%), indium(III) nitrate pentahydrate (Aldrich, 99.99%), and citric acid monohydrate (Fluka, 99%) were used as starting chemicals in the synthesis process. Aqueous solution of citric acid was added into the flask containing stoichiometric quantities of the metallic salts dissolved in distilled water. The amount of citric acid was calculated using a (citric acid)/(metal ions) molar ratio of 2:1. Then, the flask with the solution was placed in an oil bath and 25% aqueous ammonia solution was added dropwise until the pH value reached ~7. The reaction mixture was kept at 80 ℃ with constant stirring, until it started becoming viscous on account of water vaporization, and then transferred into heating calotte. The temperature was gradually increased in order to eliminate the water residue, resulting in a brownish swelling resin. At temperatures over 200 ℃, the auto-combustion reaction was initiated and resulted in voluminous ash as a product of the combustion. This procedure was repeated for each dopant concentration. Calcination of the precursor powders to obtain pure phase electrolyte powders was performed in air atmosphere for 5 h at 1050 ℃ in a tube oven. The sintering behavior was tested by dilatometric measurements from room temperature to 1350 ℃ at a rate of 5 ℃/min. Dense ceramic samples were produced

by uniaxial pressing of the powders at 150 MPa in a cylindrical die of 8 mm in diameter followed by sintering in air atmosphere for 5 h at 1100, 1200, and 1300 ℃. The densities of the samples were determined by Archimedes method, using water as a fluid.

The phase purity of the as-obtained powders was checked by X-ray diffraction (XRD; Rigaku DMax 2500 PC) analysis using a Cu Kα radiation ($\lambda_{\text{Cu K}\alpha}$ = 1.54178×10^{-10} m) from 20° to 90° 2θ angle and scanning speed of 1 (°)/min. The XRD data for sintered BCI5, BCI25, and BCI40 samples were collected from 20° to 90° 2θ with a step size of 0.02° and a counting time of 3 s. Rietveld-like refinement was performed by *Powder Cell* software in order to identify the phase composition. Unit cell parameters were calculated using *LSUCRI* program. The sintered samples were investigated by scanning electron microscopy (FE-SEM; Jeol JSM 6330F). The average grain size of the samples was determined by intercept method as described elsewhere [17,25].

Total electrical conductivity of the Pt/BaCe$_{1-x}$In$_x$O$_3$/ Pt cells was investigated by an FRA Solartron 1260 impedance analyzer coupled with a Solartron 1296 dielectric interface. Measurements were performed in 1 MHz–10 Hz frequency range between 400 and 700 ℃ in a wet hydrogen atmosphere (3 vol% H_2O) provided by letting the gas through a gas washer filled with distilled water at room temperature. During the measurements, the gas flow rate of 50 cm^3/min was kept constant by a digital mass flow controller and meter (MKS PR 4000B-F). The impedance plots were fitted using *ZView*® for *Windows* software (Version 3.2b).

Stability of the electrolyte compounds was examined in a so-called accelerated degradability test, where the sintered samples were exposed to pure CO_2 atmosphere at 700 ℃ for 5 h. The flow rate of CO_2 through the aperture was kept constant at 50 cm^3/min. After exposure, the pellets were investigated by the XRD analysis to determine possible changes in their composition.

The fuel cell testing was performed for the BCI25 electrolyte. NiO–BCI25 (1:1 weight ratio) composite powders were prepared by the method of evaporation and decomposition of solutions and suspensions (EDSS) [24]. The starting components were nickel(II) nitrate hexahydrate (Aldrich, 99.99%) and the as-prepared BCI25 powders. The resulting mixture was ground in an agate mortar and fired at 1000 ℃ for 5 h. The NiO–BCI25/BCI25 half cell was produced using the method of co-pressing. Firstly, NiO–BCI25 powders were uniaxially pressed at 70 MPa and then 10 mg of BCI25 powders were distributed on the surface of the anode pellet. In this way, NiO–BCI25/BCI25 half cell was produced by uniaxially co-pressing at 150 MPa and co-sintering at 1300 ℃ for 5 h.

Complete fuel cell was fabricated by applying commercial La$_{0.8}$Sr$_{0.2}$Co$_{0.8}$Fe$_{0.2}$O$_3$ (LSCF; Sigma-Aldrich) with 10 wt% of BCI25 as a composite cathode on the electrolyte side of the NiO–BCI25/BCI25 half cell. The cathode composite powders were mixed with printing oil to make a slurry that was brush-painted over the BCI25 electrolyte surface and then fired at 1100 ℃ for 2 h. The fuel cell tests were carried out between 550 and 700 ℃ using an Autolab PGSTAT302N (Eco Chemie BV). The anode was exposed to wet hydrogen (~3 vol% H_2O), while the cathode was exposed to ambient air. The cell was equilibrated at open-circuit for about 10 min before electrochemical measurements.

3　Results and discussion

XRD patterns were collected for all calcined BaCe$_{1-x}$In$_x$O$_{3-\delta}$ powders synthesized by the auto-combustion reaction method (Fig. 1). Main reflections of the samples referred to a perovskite structure with orthorhombic symmetry (space group *Pnma*). It was observed that small peaks of In$_2$O$_3$, as a secondary phase, appeared at In concentration above 20 mol% (not exceeding 5 wt%), while doping above 25 mol% caused noticeable splitting of the BaCeO$_3$ diffraction peaks. Traces of BaCO$_3$ phase were also detected in almost every sample according to the presence of small peaks at 23.9°.

Sintering behavior of BCI20 pellet was investigated by dilatometric measurements in order to determine optimal sintering temperature. Dilatometric curve (Fig. 2(a)) showed slow decrease in sample length with increase of temperature up to 1000 ℃, followed by sharp decrease in length between 1000 and 1100 ℃. Further increase of temperature did not cause further length shrinkage, suggesting that densification process was finished at ~1100 ℃. The final relative shrinkage was ~10%. Although the dilatometric measurement showed that temperature of 1100 ℃ is enough to reach maximal shrinkage of the BCI20 sample, the densities of around 90% were observed only for this sample and for BCI25 and BCI30, while the values for BCI5
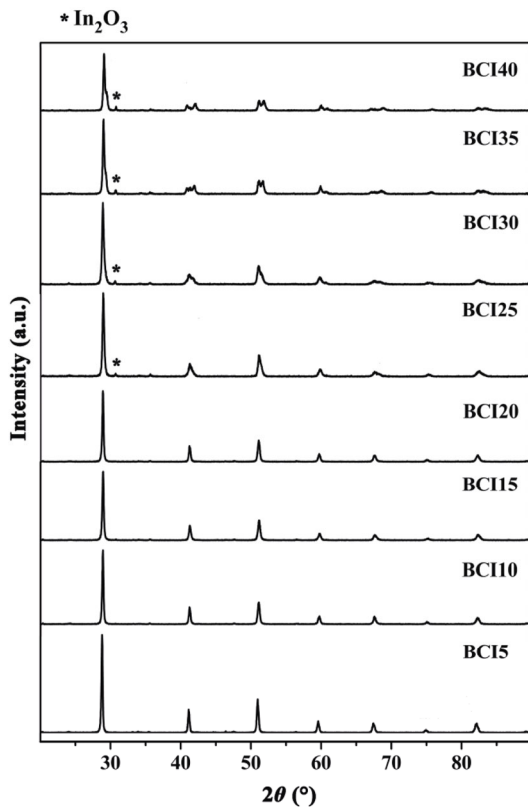
Fig. 1 XRD analysis of the In-doped BaCeO$_3$ powders calcined at 1050 ℃ for 5 h.

and BCI40 were below 70%. To ensure complete densification of the samples with other In concentrations, the sintering process was carried out at 1200 and 1300 ℃. Sintering at higher temperatures further increased the density of the obtained ceramics from ~94% at 1200 ℃ to ~96% at 1300 ℃ for BCI20 (Fig. 2(b)). Although the densities of the samples varied notably with the In concentration and the sintering temperatures, they increased gradually with indium content up to 25 mol% at observed temperature, and

thereafter started to decrease slightly. The sintering temperature of 1200 ℃ was yet insufficient for complete densification of the sample BCI5 (~88%), while at 1300 ℃ densities above 90% were obtained for all the samples. At each sintering temperature, the relative density of BCI25 sample was the highest compared with the other samples: 91% at 1100 ℃, 96% at 1200 ℃, and 98% at 1300 ℃ (Fig. 2(b)). These temperatures are markedly lower than temperatures required for sintering of BaCeO$_3$ doped by Nb, Ta, Zr, Y, or Eu, which in most cases exceeds 1400 ℃ [9,10,20,24,25,28].

The effects of different sintering temperatures on microstructure were examined by scanning electron microscopy (SEM). For comparison, the micrographs of BCI5, BCI25, and BCI40 samples' surface sintered at 1200 and 1300 ℃ are presented in Fig. 3. It can be seen from the SEM images that grain size has multimodal distribution and that it increased with increasing In concentration from 0.15–0.50 μm (BCI5) to 0.30–0.80 μm (BCI25 and BCI40) at 1200 ℃, and from 0.40–1.10 μm (BCI5) to 0.50–2.10 μm (BCI25 and BCI40) at 1300 ℃. It was expected because doping with indium improves sintering [22,23] and enhances the grain growth at lower temperatures [24,29]. By comparing the grain size for the samples sintered at different temperatures, it can be concluded that the higher sintering temperature also contributed to the formation of larger grains. It was further found that there was no change in grain size between BCI25 and BCI40 samples at observed temperatures, suggesting that increase of In concentration above 25 mol% had no significant effect either on the grain size values or the samples' microstructure in general.

Although the presence of In$_2$O$_3$ phase in BCI25 and BCI40 was not detected by backscattered electron
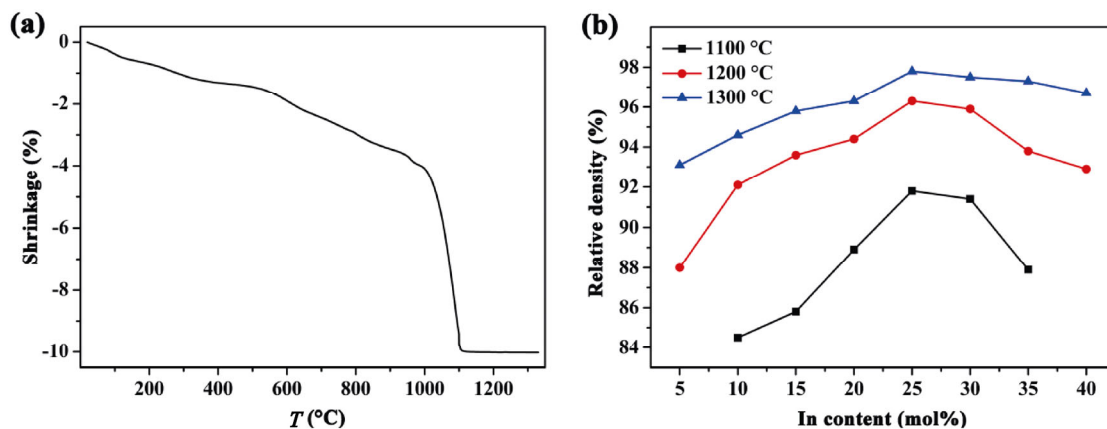

Fig. 2 Dilatometric analysis of the BCI20 sample (a), and relative densities of the samples sintered at 1100, 1200, and 1300 ℃ (b).
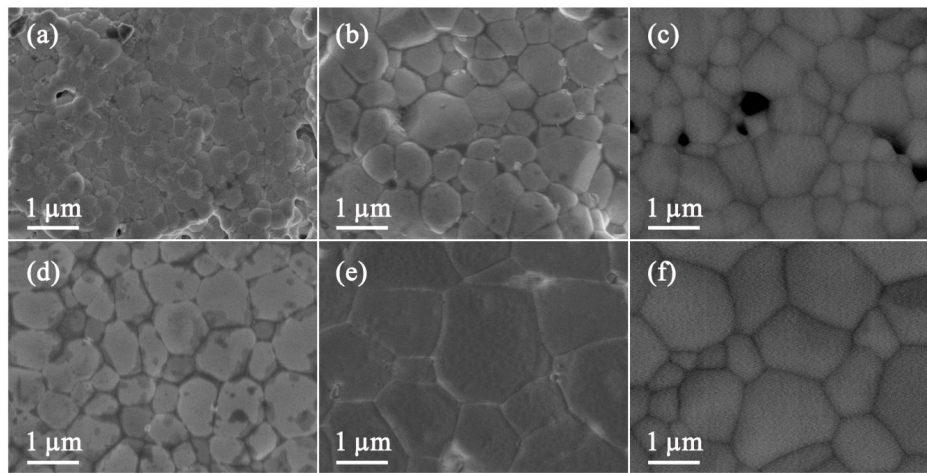
Fig. 3 SEM images of BCI5 (a), BCI25 (b), and BCI40 (c) sintered at 1200 ℃, and BCI5 (d), BCI25 (e), and BCI40 (f) sintered at 1300 ℃.

imaging (BSE) (Fig. 4(a)), it was confirmed by the XRD analysis of samples sintered at 1300 ℃ (Fig. 4(b)). The traces of $BaCO_3$ completely diminished after sintering of the samples (Fig. 4). The peaks of BaO phase, as the solid-state product of $BaCO_3$ decomposition, were not present in the XRD patterns of the sintered samples, indicating that BaO most likely was re-incorporated into $BaCe_{1-x}In_xO_{3-\delta}$ phase or evaporated during sintering. The peaks and their splitting were identified and indexed accordingly. In_2O_3 as the secondary phase appeared when In content was above 20 mol%. Also, preliminary calculated values of the unit cell volumes, obtained from the XRD analysis on the powders, monotonously decreased from ~339 $Å^3$ for BCI5 to ~328 $Å^3$ for BCI40, which is expected since In^{3+} ionic radius in octahedral environment is 0.80 Å comparing to that of Ce^{4+}, which amounts 0.87 Å. It led to the conclusion that incorporation of In into

$BaCeO_3$ lattice continued even for concentrations when In_2O_3 appeared as the secondary phase. More detailed structural analysis of the sintered samples showed that their main reflections were indexed in the orthorhombic crystal system with *Pnma* space group. The change in unit cell parameters, i.e., *a*, *b*, and *c*, does not occur simultaneously (Table 1). In other words, there was a decrease in *a* and *b* between BCI5 and BCI25, which is expected since In^{3+} ionic radius in octahedral environment is 0.80 Å comparing to that of Ce^{4+}, which amounts 0.87 Å. However, in BCI40 *a* and *c* decreased, and *b* increased comparing to BCI25. It means that BCI25 is on the limit to keep the initial unit cell proportion, whereas for concentrations above 25 mol% of In, which shares 4*b* Wyckoff position (0, 0, 1/2) with Ce^{4+}, cause the additional shrinkage along *a* and *c*. Due to the unchanged content of Ba^{2+}, which occupies 4*c* Wyckoff position (*x*, 1/4, *z*), the unit cell
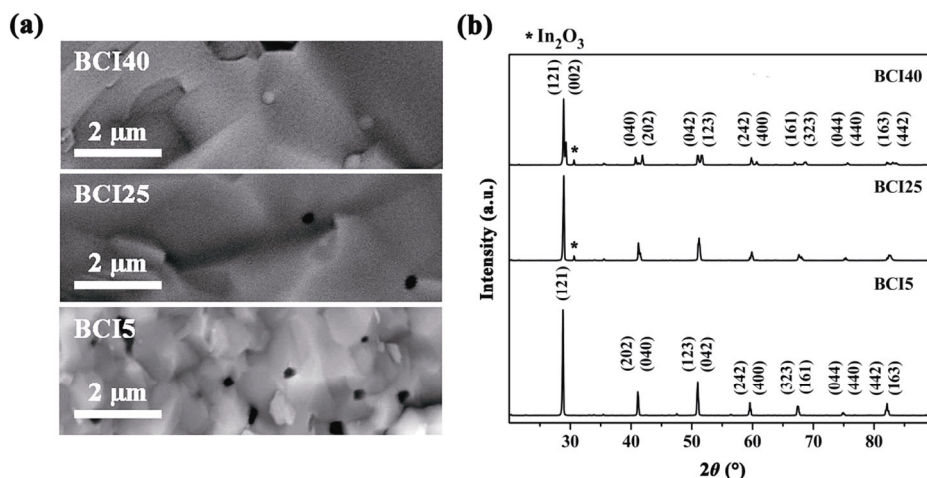

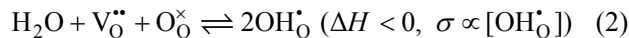**Fig. 4** BSE images (a) and XRD analysis (b) of BCI5, BCI25, and BCI40 samples sintered at 1300 ℃.
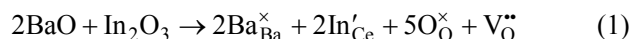
Table 1   Unit cell parameters and Goldschmidt tolerance factor (*t*) values of the samples sintered at 1300 ℃

Sample	Unit cell parameters				t^*
	a (Å)	b (Å)	c (Å)	V (Å^3)	
BCI5	6.189(3)	8.761(4)	6.228(7)	337.6(7)	0.934
BCI25	6.161(7)	8.708(9)	6.229(14)	334.1(6)	0.945
BCI40	6.095(4)	8.859(5)	6.089(5)	328.7(3)	0.949

* Theoretical value of Goldschmidt tolerance factor of In-doped BaCeO$_3$ calculated according to Eq. (3).

responds to that shrinkage by elongation along *b*. Observed splitting of diffraction peaks and shift in their positions is direct consequence of this change of the unit cell proportion.

For a more profound understanding of the relation between structure defects, microstructure, and electrical properties of the $BaCe_{1-x}In_xO_{3-\delta}$ samples sintered at 1200 and 1300 ℃, electrochemical impedance spectroscopy measurements were performed on Pt/$BaCe_{1-x}In_xO_{3-\delta}$/Pt cells under the wet hydrogen atmosphere. The total electrical conductivity, σ, of all samples increased with increase in temperature from 400 ℃ and reached maximum at 700 ℃, which is an indication of predominantly ionic type of conduction. The highest conductivity values were calculated for 700 ℃ (Fig. 5(a)) for the BCI25 sample, i.e., 0.0042 S/cm sintered at 1200 ℃ and 0.0052 S/cm sintered at 1300 ℃, somewhat lower than literature values for other proton conducting materials that usually reach ~10^{-2} S/cm [9,17,30,31]. Increase in total conductivities up to 25 mol% of In can be explained by acceptor doping mechanism expressed by Kröger–Vink notation, expressed by Eqs. (1) and (2):

$$2BaO + In_2O_3 \rightarrow 2Ba_{Ba}^{\times} + 2In_{Ce}' + 5O_O^{\times} + V_O^{\bullet\bullet} \tag{1}$$

$$H_2O + V_O^{\bullet\bullet} + O_O^{\times} \rightleftharpoons 2OH_O^{\bullet} \ (\Delta H < 0, \ \sigma \propto [OH_O^{\bullet}]) \tag{2}$$

However, the greater conductivity values for the samples sintered at 1300 ℃ comparing to those sintered at 1200 ℃ could be attributed to the difference in microstructure and higher densities for samples sintered at higher temperatures. The impedance spectra presented in the inset of Fig. 5(a) were fitted by a model circuit consisting of stray inductance (*L*), resistors (R_1, R_2, and R_3), constant phase element (CPE), and Warburg element (*W*). The effective capacitances were calculated from the formula $C = (Q \cdot R_2)^{1/n}/R_2$, where Q and n represent constants of CPE. These values ranged within 10^{-6} F/cm in the temperature range between 500 and 700 ℃, which were typical for processes on the electrode surface [10,16]. The part of the model circuit consisting of Warburg element is related to mass transfer phenomena near electrode surface [32,33]. Therefore, in 500–700 ℃ temperature range, the contributions of the bulk and grain boundaries were not separable and only the total conductivity values were considered (R_1). These values were calculated according to the formula $\sigma = 1/R_1 \cdot l/S$, where *l* represents the thickness and *S* the surface area of the pellet. The total conductivities of the BCI25 electrolyte sintered at 1200 and 1300 ℃ in form of Arrhenius plot are presented in Fig. 5(b). Both activation energy values obtained from the slope, 0.31 and 0.33 eV for samples sintered at 1200 and 1300 ℃ respectively, were in the range for proton conduction for doped BaCeO$_3$ [9,11].

The conductivities for higher In concentrations ($\geqslant$ 25 mol%) depended on two opposed effects: the unit
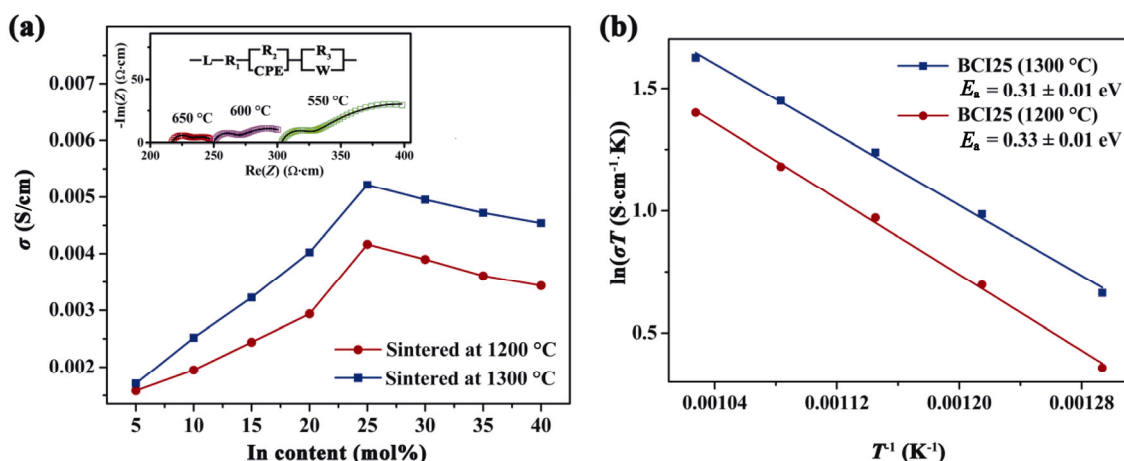

Fig. 5 Total conductivities at 700 ℃ of BCI5–BCI40 samples sintered at 1200 and 1300 ℃ with examples of impedance spectra of BCI25 sample sintered at 1300 ℃ (a), and temperature dependence of total conductivities in form of Arrhenius plots of BCI25 electrolytes sintered at 1200 and 1300 ℃ (b).

cell shrinkage and the increase in concentration of the protonic defects, whereas the unit cell shrinkage had the prevailing influence. Therefore, the total conductivities slightly decreased when the concentration of In increased from 25 to 40 mol%. Other aspects that may contribute to the drop in conductivity are: formation of defect clusters [29,34], reduced symmetry as indicated by the values of the unit cell parameters and peak splitting [10,15,16], somewhat lower density values and formation of In_2O_3 as the secondary phase, which lacks proton conducting ability. However, this drop in total conductivity was not so pronounced since the total conductivities of the samples BCI30, BCI35, and BCI40 were still higher than those of the samples with In content lower than 20 mol%. Bi *et al.* [22] also reported the highest conductivity of the sample with 30 mol% In by comparing the $BaCeO_3$ samples with 10, 20, and 30 mol% In, although here it was demonstrated that conductivity peak can be reached at around 25 mol%. Compared with other trivalent dopants, such as Y and rare earths [9,10,15–17,24–26], doping with In inevitably leads to a notable drop in conductivity even up to one order of magnitude. This is a consequence of its relatively higher electronegativity compared to the dopants mentioned above.

As poisoning with CO_2 is the main drawback of $BaCeO_3$ [10,31,34], the influence of In on the chemical stability was investigated for the BCI15, BCI20, and BCI25 samples sintered at 1300 ℃ by exposing them to the pure CO_2 atmosphere at 700 ℃ for 6 h. By comparing the XRD patterns before and after CO_2 exposure (Fig. 6), minor peak at around 24° 2θ, which indicates the traces of $BaCO_3$ phase, was found for BCI15 and BCI20 and not for BCI25. Increased

chemical stability of In-doped samples could be explained using Goldschmidt tolerance factor defined for $BaCe_{1-x}In_xO_{3-\delta}$ (Eq. (3)), where r is the ionic radius and the Roman numerals in the subscript represent their coordination number [17,18,35].

$$t = \frac{r\left(Ba_{XII}^{2+}\right) + r\left(O_{VI}^{2-}\right)}{\sqrt{2}\left[(1-x)\cdot r\left(Ce_{VI}^{4+}\right) + x\cdot r\left(In_{VI}^{3+}\right) + r\left(O_{VI}^{2-}\right)\right]} \quad (3)$$

Normally, the calculated values for t increased with In concentration as presented in Table 1. The closer t is to unity, the more stable the perovskite lattice is, and thus substitution of Ce by In which has smaller ionic radius improves chemical stability of $BaCeO_3$ [29]. According to the literature, doping with In increases the stability of lattice by increasing its acidic character due to its higher electronegativity (1.78) than cerium (1.12) [24,36]. The advantage of using indium over other dopants with high electronegativity, such as Nb^{5+}, Ta^{5+}, or Zr^{4+}, is that, as a trivalent ion, In^{3+} allows formation of oxygen vacancies. Also, similar values of the In and Ce ionic radii provide incorporation of In in the crystal lattice of $BaCeO_3$ up to 20–25 mol%. However, the so-called "trade-off" relationship between chemical stability and conductivity was once again confirmed in the case of In-doped $BaCeO_3$, since basicity of the crystal lattice is vital for proton conducting mechanism [21], making it vulnerable to CO_2 and vice versa.

According to the results presented above, we found that BCI25 sample was the best choice for electrolyte compared with the other investigated samples as it exhibited the highest proton conductivity and stability in CO_2 environment. Therefore, it was chosen for the fuel cell fabrication, characterization, and testing using
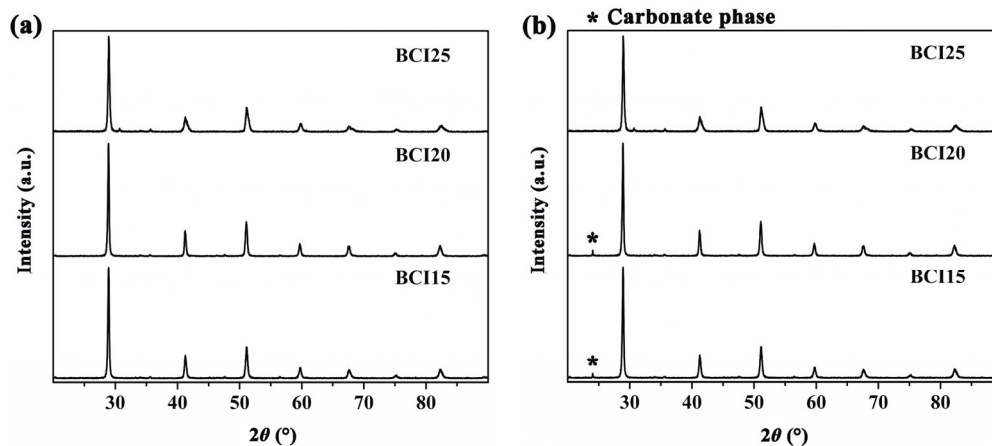

Fig. 6 XRD patterns of the pellets sintered in air at 1300 ℃ before (a) and after (b) being exposed to the CO_2 atmosphere for 5 h at 700 ℃.

an anode-supported configuration consisting of Ni–BCI25 cermet for the anode and LCSF–BCI25 for the cathode.

BSE image of NiO–BCI25 anode pellet is shown in Fig. 7(a). Distribution of NiO and BCI25 grains was uniform in a considerably porous microstructure, which is essential for the functionality of the anode. Such distribution provides a continuous triple phase boundary between metallic nickel, electrolyte, and gaseous hydrogen, facilitating efficient hydrogen oxidation and proton transport throughout the whole volume of the anode. XRD pattern of the anode pellet (Fig. 7(b)) contained only peaks belonging to NiO and BCI25 phases, suggesting that NiO and BCI25 were mostly chemically compatible during the sintering at 1300 ℃. However, by analyzing XRD patterns of both BCI25 and BCI25–NiO composites, a small decrease in unit cell volume was observed (0.6 Å^3), suggesting that nickel was partially incorporated into the perovskite structure [11,37,38]. Thus, a slight decrease of the ionic part of the anode conductivity can be expected.

Power outputs and *I–V* characteristics (Fig. 8(a)) were obtained by exposing the anode to wet hydrogen and the cathode to ambient air in 550–700 ℃ temperature range. The measured values of open circuit cell potential difference (ΔE) were close to and slightly lower than the calculated ones (ΔE_{calc}) (Table 2), which was the proof of the dense and gas-tight electrolyte. This difference is mainly a consequence of the ohmic resistance of the electrolyte, while somewhat

higher decrease in ΔE value at 700 ℃ can be ascribed to eventual short circuiting trough the electrolyte and higher electrode overpotentials [39,40]. Maximum power density outputs increased with the temperature, reaching 264 mW/cm^2 (Table 2) at 700 ℃, which is comparable with the results found in literature [41]. High power output in the whole 550–700 ℃ temperature range is the consequence of dense microstructure and high conductivity of BCI25 sintered at 1300 ℃, caused by the presence of larger grains and accordingly minor blocking effect of grain boundaries on the proton conductivity.

By examining the micrograph of a cross section of fuel cell after electrochemical measurement (Fig. 8(b)), no signs of degradation were noticed. The anode, electrolyte, and cathode layers were clearly distinguishable. A thin layer of electrolyte of 20–25 μm contributed to a low ohmic resistivity, which resulted in relatively high power output comparable with the literature data for similar SOFC configurations [23,24]. Both cathode–electrolyte and anode–electrolyte interfaces showed good interfacial adhesion as well.

4   Conclusions

Chemical stability and functionality of BaCe$_{1-x}$In$_x$O$_{3-\delta}$ as an electrolyte for SOFC were investigated in wider dopant concentration range. Based on XRD,
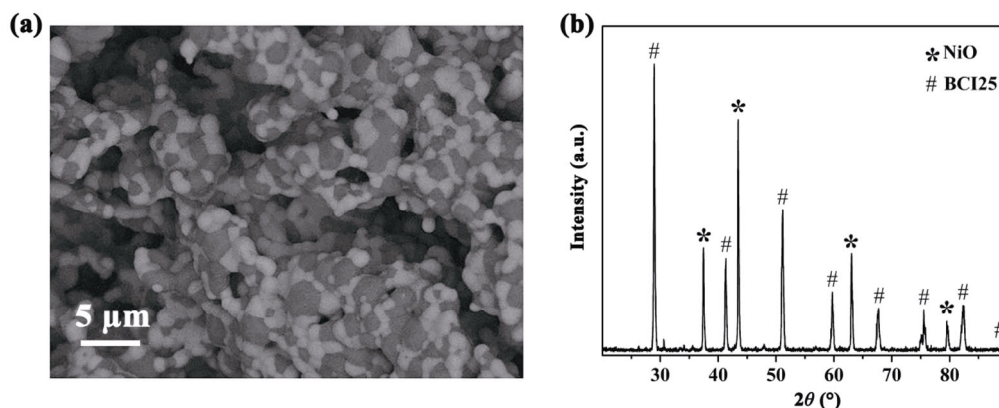

Fig. 7   BSE image (a) and XRD pattern (b) of NiO–BCI25 (1:1 weight ratio) anode sintered at 1300 ℃.

Table 2   Calculated (ΔE_{calc}) and measured (ΔE) open circuit cell potential differences and maximum power outputs for fuel cell measured in the 550–700 ℃ temperature range

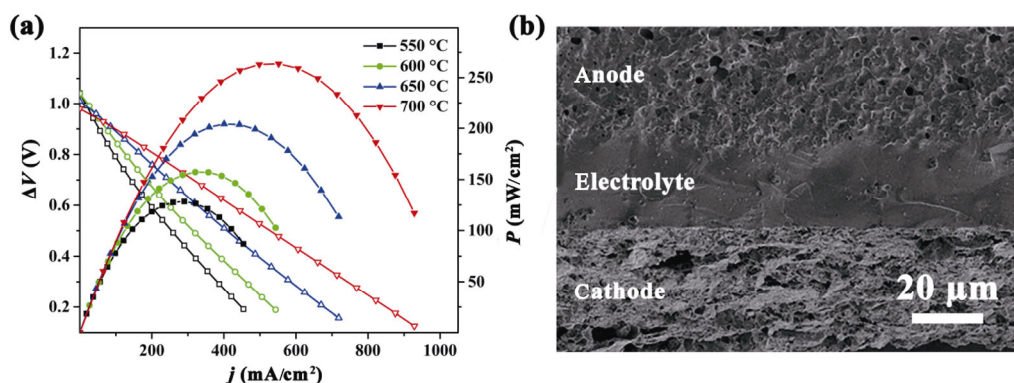|	550 ℃	600 ℃	650 ℃	700 ℃
ΔE_{calc} (V)	1.12	1.11	1.10	1.10
ΔE (V)	1.05	1.04	1.02	0.98
P (mW/cm^2)	126	157	207	264

Fig. 8 *I–V* curves and power outputs of Ni–BCI25/BCI25/LSCF–BCI25 cell with electrolyte sintered at 1300 ℃ measured in 550–700 ℃ range (a), and the cross-sectional view of cell after testing the prototype cell (b).

$BaCe_{1-x}In_xO_{3-\delta}$ samples with perovskite structure (space group *Pnma*) were obtained by the auto-combustion reaction. The sample with 25 mol% In, sintered at 1300 ℃, proved to be the best choice as an electrolyte material. It exhibited the highest total conductivity values in the whole temperature range. By examining and comparing the results of the XRD, SEM analyses, and conductivity values, it was found that amount of In in $BaCeO_3$ lattice increased even above the concentration of 25 mol% and caused the distortion of the unit cell proportions. Further increase in In concentration led to formation of In_2O_3 as the secondary phase without proton conducting ability. The presence of secondary phase, lower densities, decrease in unit cell volume, and change in unit cell proportions contributed to certain drop in total conductivity for samples with > 25 mol% of In. Additionally, higher concentrations of In (> 25 mol%) no longer contributed to the sinterability of the ceramics. In general, In proved to be a good choice for doping $BaCeO_3$ because it lowers the sintering temperature and enhances its stability in CO_2 atmosphere, as confirmed by XRD analysis. On the other hand, lower conductivity of $BaCe_{1-x}In_xO_{3-\delta}$ could be compensated by application of a thin electrolyte layer in the anode-supported configuration. It was enabled by the auto-combustion synthesis method of electrolyte powders with high specific surface area that facilitate fabrication of functional electrolyte and electrode materials. Thus, the fuel cell Ni–BCI25/BCI25/LSCF–BCI25 sintered at 1300 ℃ reached maximum power density of 264 mW/cm^2 at 700 ℃, comparable with the optimal results found in literature. Further improvements can be made by using a configuration that consists of more stable, i.e., BCI25-based anode and cathode composites, while $BaCeO_3$-based electrolyte as protected by these layers may contain dopants that promote higher proton conductivity than In does.

References

[1] Iwahara H, Esaka T, Sato T, *et al*. Formation of high oxide ion conductive phases in the sintered oxides of the system Bi_2O_3–Ln_2O_3 (Ln = La–Yb). *J Solid State Chem* 1981, **39**: 173–180.

[2] Iwahara H, Esaka T, Uchida H, *et al*. Proton conduction in sintered oxides and its application to steam electrolysis for hydrogen production. *Solid State Ion* 1981, **3–4**: 359–363.

[3] Mitsui A, Miyayama M, Yanagida H. Evaluation of the activation energy for proton conduction in perovskite-type oxides. *Solid State Ion* 1987, **22**: 213–217.

[4] Iwahara H, Uchida H, Ono K, *et al*. Proton conduction in sintered oxides based on $BaCeO_3$. *J Electrochem Soc* 1988, **135**: 529–533.

[5] Shi Z, Sun W, Wang Z, *et al*. Samarium and yttrium codoped $BaCeO_3$ proton conductor with improved sinterability and higher electrical conductivity. *ACS Appl Mater Interfaces* 2014, **6**: 5175–5182.

[6] Su XT, Yan QZ, Ma XH, *et al*. Effect of co-dopant addition on the properties of yttrium and neodymium doped barium cerate electrolyte. *Solid State Ion* 2006, **177**: 1041–1045.

[7] Wang S, Shen JX, Zhu ZW, *et al*. Further optimization of barium cerate properties via co-doping strategy for potential application as proton-conducting solid oxide fuel cell electrolyte. *J Power Sources* 2018, **387**: 24–32.

[8] Petit CTG, Tao SW. Structure and conductivity of praseodymium and yttrium co-doped barium cerates. *Solid State Sci* 2013, **17**: 115–121.

[9] Radojković A, Žunić M, Savić SM, *et al*. Enhanced stability in CO_2 of Ta doped $BaCe_{0.9}Y_{0.1}O_{3-\delta}$ electrolyte for intermediate temperature SOFCs. *Ceram Int* 2013, **39**: 2631–2637.

[10] Radojković A, Žunić M, Savić SM, *et al*. Chemical stability and electrical properties of Nb doped $BaCe_{0.9}Y_{0.1}O_{3-\delta}$ as a high temperature proton conducting electrolyte for IT-SOFC. *Ceram Int* 2013, **39**: 307–313.

[11] Gdula-Kasica K, Mielewczyk-Gryn A, Molin S, *et al*. Optimization of microstructure and properties of acceptor-doped barium cerate. *Solid State Ion* 2012, **225**: 245–249.

[12] Di Bartolomeo E, D'Epifanio A, Pugnalini C, *et al*. Structural analysis, phase stability and electrochemical characterization of Nb doped $BaCe_{0.9}Y_{0.1}O_{3-x}$ electrolyte for IT-SOFCs. *J Power Sources* 2012, **199**: 201–206.

[13] Babu AS, Bauri R. Synthesis, phase stability and conduction behavior of rare earth and transition elements doped barium cerates. *Int J Hydrog Energy* 2014, **39**: 14487–14495.

[14] Kreuer K-D, Paddison SJ, Spohr E, *et al*. Transport in proton conductors for fuel-cell applications: Simulations, elementary reactions, and phenomenology. *Chem Rev* 2004, **104**: 4637–4678.

[15] Amsif M, Marrero-Lopez D, Ruiz-Morales JC, *et al*. Influence of rare-earth doping on the microstructure and conductivity of $BaCe_{0.9}Ln_{0.1}O_{3-\delta}$ proton conductors. *J Power Sources* 2011, **196**: 3461–3469.

[16] Amsif M, Marrero-López D, Ruiz-Morales JC, *et al*. Effect of sintering aids on the conductivity of $BaCe_{0.9}Ln_{0.1}O_{3-\delta}$. *J Power Sources* 2011, **196**: 9154–9163.

[17] Radojković A, Žunić M, Savić SM, *et al*. Co-doping as a strategy for tailoring the electrolyte properties of $BaCe_{0.9}Y_{0.1}O_{3-\delta}$. *Ceram Int* 2019, **45**: 8279–8285.

[18] Medvedev DA, Lyagaeva JG, Gorbova EV, *et al*. Advanced materials for SOFC application: Strategies for the development of highly conductive and stable solid oxide proton electrolytes. *Prog Mater Sci* 2016, **75**: 38–79.

[19] Zuo CD, Lee TH, Dorris SE, *et al*. Composite Ni–Ba $(Zr_{0.1}Ce_{0.7}Y_{0.2})O_3$ membrane for hydrogen separation. *J Power Sources* 2006, **159**: 1291–1295.

[20] Hakim M, Joo JH, Yoo CY, *et al*. Enhanced chemical stability and sinterability of refined proton-conducting perovskite: Case study of $BaCe_{0.5}Zr_{0.3}Y_{0.2}O_{3-\delta}$. *J Eur Ceram Soc* 2015, **35**: 1855–1863.

[21] Kreuer KD. On the development of proton conducting materials for technological applications. *Solid State Ion* 1997, **97**: 1–15.

[22] Bi L, Tao ZT, Liu C, *et al*. Fabrication and characterization of easily sintered and stable anode-supported proton-conducting membranes. *J Membr Sci* 2009, **336**: 1–6.

[23] Bi L, Zhang SQ, Zhang L, *et al*. Indium as an ideal functional dopant for a proton-conducting solid oxide fuel cell. *Int J Hydrog Energy* 2009, **34**: 2421–2425.

[24] Žunić M, Branković G, Foschini CR, *et al*. Influence of the indium concentration on microstructural and electrical properties of proton conducting $NiO–BaCe_{0.9-x}In_xY_{0.1}O_{3-\delta}$

cermet anodes for IT-SOFC application. *J Alloys Compd* 2013, **563**: 254–260.

[25] Radojković A, Savić SM, Pršić S, *et al*. Improved electrical properties of Nb doped $BaCe_{0.9}Y_{0.1}O_{2.95}$ electrolyte for intermediate temperature SOFCs obtained by auto-combustion method. *J Alloys Compd* 2014, **583**: 278–284.

[26] Žunić M, Chevallier L, Radojković A, *et al*. Influence of the ratio between Ni and $BaCe_{0.9}Y_{0.1}O_{3-\delta}$ on microstructural and electrical properties of proton conducting Ni–$BaCe_{0.9}Y_{0.1}O_{3-\delta}$ anodes. *J Alloys Compd* 2011, **509**: 1157–1162.

[27] Dias PAN, Nasani N, Horozov TS, *et al*. Non-aqueous stabilized suspensions of $BaZr_{0.85}Y_{0.15}O_{3-\delta}$ proton conducting electrolyte powders for thin film preparation. *J Eur Ceram Soc* 2013, **33**: 1833–1840.

[28] Radojković A, Savić SM, Jović N, *et al*. Structural and electrical properties of $BaCe_{0.9}Ee_{0.1}O_{2.95}$ electrolyte for IT-SOFCs. *Electrochimica Acta* 2015, **161**: 153–158.

[29] Yang SJ, Wen YB, Zhang SP, *et al*. Performance and stability of $BaCe_{0.8-x}Zr_{0.2}In_xO_{3-\delta}$-based materials and reversible solid oxide cells working at intermediate temperature. *Int J Hydrog Energy* 2017, **42**: 28549–28558.

[30] Wang YZ, Huang J, Su TT, *et al*. Synthesis, microstructure and electrical properties of $BaZr_{0.9}Y_{0.1}O_{3-\delta}$: $BaCe_{0.86}Y_{0.1}Zn_{0.04}O_{3-\delta}$ proton conductors. *Mater Sci Eng*: *B* 2015, **196**: 35–39.

[31] Zakowsky N, Williamson S, Irvine JTS. Elaboration of CO_2 tolerance limits of $BaCe_{0.9}Y_{0.1}O_{3-\delta}$ electrolytes for fuel cells and other applications. *Solid State Ion* 2005, **176**: 3019–3026.

[32] Slade RCT, Flint SD, Singh N. AC and DC electrochemical investigation of protonic conduction in calcium-doped barium cerate ceramics. *J Mater Chem* 1994, **4**: 509–513.

[33] Khandelwal M, Venkatasubramanian A, Prasanna TRS, *et al*. Correlation between microstructure and electrical conductivity in composite electrolytes containing Gd-doped ceria and Gd-doped barium cerate. *J Eur Ceram Soc* 2011, **31**: 559–568.

[34] Ryu KH, Haile SM. Chemical stability and proton conductivity of doped $BaCeO_3$–$BaZrO_3$ solid solutions. *Solid State Ion* 1999, **125**: 355–367.

[35] Bhide SV, Virkar AV. Stability of $AB'_{1/2}B''_{1/2}O_3$-type mixed perovskite proton conductors. *J Electrochem Soc* 1999, **146**: 4386–4392.

[36] Giannici F, Longo A, Balerna A, *et al*. Indium doping in barium cerate: The relation between local symmetry and the formation and mobility of protonic defects. *Chem Mater* 2007, **19**: 5714–5720.

[37] Abdul Malik L, Mahmud NA, Mohd Affandi NS, *et al*. Effect of nickel oxide - Modified $BaCe_{0.54}Zr_{0.36}Y_{0.1}O_{2.95}$ as composite anode on the performance of proton-conducting solid oxide fuel cell. *Int J Hydrog Energy* 2021, **46**: 5963–5974.

[38] Shimada H, Yamaguchi T, Sumi H, *et al*. Effect of Ni diffusion into $BaZr_{0.1}Ce_{0.7}Y_{0.1}Yb_{0.1}O_{3-\delta}$ electrolyte during

high temperature co-sintering in anode-supported solid oxide fuel cells. *Ceram Int* 2018, **44**: 3134–3140.

[39] Žunić M, Chevallier L, Di Bartolomeo E, *et al*. Anode supported protonic solid oxide fuel cells fabricated using electrophoretic deposition. *Fuel Cells* 2011, **11**: 165–171.

[40] Meng XX, Yang NT, Song J, *et al*. Synthesis and characterization of terbium doped barium cerates as a proton conducting SOFC electrolyte. *Int J Hydrog Energy* 2011, **36**: 13067–13072.

[41] Medvedev D, Murashkina A, Pikalova E, *et al*. $BaCeO_3$: Materials development, properties and application. *Prog Mater Sci* 2014, **60**: 72–129.